



HAL
open science

Transition from ballistic to thermalized transport of the metal sputtered species in DC magnetron

Adrien Revel, Abderzak El Farsy, Ludovic de Poucques, Jacques Robert,
Tiberiu Minea

► To cite this version:

Adrien Revel, Abderzak El Farsy, Ludovic de Poucques, Jacques Robert, Tiberiu Minea. Transition from ballistic to thermalized transport of the metal sputtered species in DC magnetron. Plasma Sources Science and Technology, 2021, 10.1088/1361-6595/ac352b . hal-03473421

HAL Id: hal-03473421

<https://hal.science/hal-03473421>

Submitted on 9 Dec 2021

HAL is a multi-disciplinary open access archive for the deposit and dissemination of scientific research documents, whether they are published or not. The documents may come from teaching and research institutions in France or abroad, or from public or private research centers.

L'archive ouverte pluridisciplinaire **HAL**, est destinée au dépôt et à la diffusion de documents scientifiques de niveau recherche, publiés ou non, émanant des établissements d'enseignement et de recherche français ou étrangers, des laboratoires publics ou privés.



Distributed under a Creative Commons Attribution - NonCommercial - NoDerivatives 4.0
International License

Transition from ballistic to thermalized transport of the metal sputtered species in DC magnetron

Adrien Revel^{1,2}, Abderzak el Farsy^{1,2,*}, Ludovic de Poucques²,
Jacques Robert¹, Tiberiu Minea¹

June 2021

¹ Université Paris-Saclay, CNRS, Laboratoire de physique des gaz et des plasmas,
91405 Orsay, France

² Université de Lorraine, CNRS, IJL, F-54000 Nancy, France

***Corresponding author:** abderzak.el-farsy@universite-paris-saclay.fr, adrien.revel@universite-paris-saclay.fr

Abstract

Tunable Diode Laser Induced Fluorescence (TD-LIF) technique has been optimized to accurately measure the titanium (Ti) sputtered Atoms Velocity Distribution Functions (AVDF) in a magnetron discharge operating in Direct Current (DC) mode. The high spatial and spectral resolution achieved unveils some features of the transport of the metal sputtered atoms and their thermalization. The two groups of thermalized and energetic atoms have been very well separated compared to previous works. Hence, the fitting of the energetic atoms group shows dumping from modified Thompson to Gauss distribution when the product pressure-distance from the target increases. In parallel, sputtered metal transport from the target has been simulated using the Monte Carlo collision (MCC) approach. The direct comparison between numerical and experimental results led to an improved cross section for Titanium - Argon momentum transfer, based on the *ab initio* formulae of the interaction potential derived from noble gases interaction. The numerical parametric study of the angular distribution and cut-off energy for the initial distribution of sputtered atoms steered to a precise characterization of the initial conditions, allowed by the accuracy of experimental data. A very good overall agreement is obtained for measured and calculated AVDFs. The confrontation between measured and modeling results emphasized the major role played by the argon ions not only in the sputtering process but also in the neutral metal transport, by the gas rarefaction near the target. The microscopic description provided by the MCC model clearly reveals different transport regimes: ballistic, diffusive, and back-scattering and brings new insights on the thermalization of sputtered species in the intermediate pressure range.

Keywords: DC magnetron sputtering, tunable diode laser induced fluorescence, MCC model, sputtered atoms velocity distribution function

1 Introduction

Magnetron sputtering is worldwide used for thin film deposition. The energy and the flux of atoms or ions arriving at the substrate are of major importance for tailoring the forming film properties such as microstructure, stress, adhesion, electrical resistivity, and stoichiometry as well as the crystalline

properties [1, 2, 3]. In fact, the energy of deposited particles directly affects the elementary processes (adsorption, diffusion) of film growth. The sputtered particles, as neutrals, leave the target with relatively high energy (a few eV compared to the plasma/buffer gas, which typically has tenths of meV) and they lose energy *via* collisions with the buffer gas before reaching the substrate, which increases the fraction of thermalized atoms [4, 5, 6, 7]. This is crucial especially in conventional magnetron where the fraction of ionized sputtered species stays very low (below 1%) compared to High Power Impulse Magnetron Sputtering (HiPIMS), where this fraction can easily exceed 50%.

In the sputtering process, the transport of neutral atoms of metallic vapor has been numerically simulated and tracked for different target materials using several models. Most of them exploited Monte Carlo (MC) approach. The ejected particles from the target have an initial anisotropic energy distribution, well described by Stepanova and Dew [8]. During their transport from the target to the substrate, the sputtered atoms relax towards an equilibrium distribution continuously losing energy in interactions with the buffer gas. Many of these MC models have shown the thermalization of sputtered atoms [9, 10, 11, 12, 13]. Other models aimed to be predictive, such as SIMTRA developed by Van Aeken *et al.* [14]. It simulates the metal flux from a rotating cylindrical magnetron, but it was adjusted with respect to the measured deposition rate of thin films. SIMTRA was successfully used also to study the effect of the nature of the buffer gas on the transport of sputtered atoms as well as to predict the composition of the film when combining different metal sources, *e.g.* segmented targets or combinatorial synthesis of thin films [15]. The 3D Monte Carlo model called SPaTinG was used by Caillard *et al.* [16] to simulate the deposition by radio frequency plasma sputtering. Again, the angular distribution of the ejected atoms and the condensation coefficient onto the substrate were estimated by adjusting the simulated and experimental deposition rates. However, as most of the MC models, they are all dependent of the force field describing the interaction between the involved species. Most of these models exploit general interaction potentials (*e.g.* Morse) between the sputtered atoms (usually metal) and the buffer gas (usually argon), or even the well-known argon-argon cross section [17, 18]. Even if they well capture the trend, they are often adjusted for the quantitative simulation of the thin film growth, but without focusing on the detailed description of the metal-gas specificity, namely the momentum transfer cross section. Lundin *et al.* [5] have developed OMEGA code to simulate direct current magnetron sputtering process. They reported the first results combining the microscopic MC simulation of the sputtered atoms transport with the measured Atoms Velocity Distribution Functions (AVDF) by laser induced fluorescence at different locations in front of the target and following two orthogonal directions and different pressures. They have demonstrated the typical empirical adjustment of the metal-argon cross section fails, as it is generally taken from argon-argon cross section but weighted by the metal to argon mass ratio [18]. Hence, they proposed an empirical differential cross section for titanium - argon elastic collisions. The fitting of the experimental results [19] have shown the titanium-argon cross section is a few times higher [5] than argon-argon cross section, generally used, as mentioned before. A review of argon-argon interaction has been published by Phelps [20]. It used the quantum description of the interaction potential described as an infinite series of terms (see section 2.2) and generalized this potential for hetero-atoms interactions, as for magnetron sputtered species traveling in argon.

From this short review of the MC simulations dealing with the sputtered metal transport in magnetron discharges, the general MC paradigm is revealed. Indeed, the main limitation of MC models is the lack of self-consistency, *i.e.*, they are fully dependent of the used force field. Several issues are present in the literature, but the most common are: *ab initio* definition of the interaction potential [21]; the use of a general potential (*e.g.* Morse) [14]; the parametric study of these potentials to fit experimental data (macroscopic [15] or microscopic[5]); and the pure numerical simulation combining two approaches: (i) first the force field is obtained as a result from a self-consistent modeling (*e.g.*

Particle-in-Cell), and in a second time (ii) MC algorithm is run using the previous results for the field, so-called *a posteriori* Monte Carlo [22]. Another approach combining the force calculation and Monte Carlo algorithm is Direct Simulation Monte Carlo (DSMC) [23]. In the present work, we propose a combination of two manners to obtain the interaction cross section between titanium and argon (Ti-Ar), using the *ab initio* approach for the interaction potential following the Phelps approach [20] and the detailed microscopic information on the velocity distribution of metal atoms in the discharge experimentally recorded. It is worth mentioning the accuracy of the chosen method relies on the reliability of the AVDFs measurements.

Magnetron discharge is very inhomogeneous in space due to the magnetic field topology in front of the target (bent field lines, strong gradients, etc.) and the crossed fields configuration, magnetic and electric, perpendicular to each other in the racetrack region, and almost parallel in the center and on the edge of the target. Then, diagnostic techniques, with high spatial resolution, are required to well characterize AVDF in this kind of discharge. As a non-intrusive technique, optical emission spectroscopy is easy to implement, but it has important drawbacks, both spatial and spectral [24, 25]. Moreover, this technique only probes the radiative levels of the species [24, 26] whereas most of the species involved in the film growth are in the fundamental and metastable states. As these radiative levels are very sensitive to the plasma parameters [27], it is very difficult to evaluate their relation with the ground state. It can be done using much more sophisticated modeling schemes such as Collisional Radiative Model [28, 29]. On the contrary, Tunable Diode Laser Induced Fluorescence (TD-LIF) technique fills these requirements, and it was used here. It offers a good space resolution (of the order of a few mm^3) [7] and a very good time resolution (below $1 \mu\text{s}$) [30, 19]. Therefore, it is highly suitable to study the inhomogeneity of the densities and the fluxes from the target to the substrate, with high spectral resolution and relatively wide scanning range of wavelength (about 18 GHz without hope mode). TD-LIF allows probing all populations of sputtered atoms, even if they spread over a wide range (up to 8 km/s) [4, 6, 31]. Thus, with a theoretical adjustment procedure (see section 2.1), we can distinguish the different groups of particles that correspond to the energetic (most of them performing a "ballistic" or collisionless transport) after the ejection from the target, which survive as long as they are not interacting with the buffer gas, and those that underwent collisions evolving towards thermal population. The full thermalization process (number of collisions required, the distance from the target when the thermalization is fulfilled, etc.) is still an open issue in many systems operating in the intermediate pressure regime (low collisionality), as it is the case in conventional magnetron discharge, taken here as a use case. The intermediate pressure regime is characterized by a reduced number of collisions between the target and the substrate. The energetic species, therefore, lose some of their kinetic energy and are likely to deviate from their initial trajectory, but the number of collisions is not sufficient to lead to a fully thermalized population. This intermediate pressure regime is often used for thin film deposition, due to the higher current operation.

The goal of the present work is to develop a model capable of reproducing the AVDF of the sputtered titanium measured by TD-LIF in DC magnetron discharge. Lundin *et al.* could adjust the Ar-Ar interaction cross section [5], correcting the Somekh' empirical suggestion [18] and proposing a novel cross section for Ti-Ar interaction, much higher than the previous one. We performed the first run with this cross section from [5], but the numerically found AVDF was in disagreement with the accurately measured curve, especially for velocities around zero. The improved experimental setup gave a smoother signal and, hence, a much better description of the AVDF.

First, the experimental setup and the TD-LIF technique used in the present work are explained and the main results of the gas temperature measurements as well as the fitting procedure of the AVDF are given. Then, the numerical model background is described particularly the Monte Carlo Collision (MCC) technique. The interaction cross section has been evaluated from *ab initio* description of the

interaction potential and a parametric study converged to the initial conditions (angular and energy distribution) for sputtered particles. All these highly improved the accuracy of the model. Finally, the results are presented and the good agreement between the model and the detailed experimental data is taken as a validation for the improved interaction cross section proposed here for titanium-argon momentum exchange. In addition, a discussion about the elastic scattering process revealed three transport regimes and gave a precise evaluation of the number of collisions necessary to reach the thermodynamics equilibrium, *i.e.*, the sputtered particles become fully thermalized. Besides, an estimation is given for the weak metal back-stream of sputtered atoms returning to the cathode. Notice these atoms are not sensitive to electric and magnetic fields, and the back-scattering is a side effect of the metal-gas interactions in conventional magnetron discharge.

2 Experimental setup and Model description

2.1 Tuneable Diode Laser Induced Fluorescence

The experiments have been carried out in a reactor described in detail elsewhere [4, 32, 31]. Briefly, a titanium target (99.9%) of 5 cm in diameter was used as cathode in a planar circular balanced magnetron. The vacuum pressure was below $2 \cdot 10^{-4}$ Pa, obtained by a turbomolecular pump. The argon flow rate was fixed to 18 sccm and the operating pressure was controlled by a butterfly valve placed between the pump and the chamber. Titanium AVDFs are measured at two pressures of 0.4 Pa and 1.3 Pa. The magnetron discharge was operated in direct current (DC) mode with a typical voltage of 300 V and a mean discharge power of 5 Wcm^{-2} , corresponding to 100 W over the whole target area.

The optical configuration of TD-LIF is very similar to that used in [32]. The tuneable diode laser (Toptica Photonics DL 100) allows scanning 9 pm wavelength range with locked single mode. For titanium, we used the same absorption transition as in previous work [5] and the fluorescence signal (λ_{LIF}) was detected at $\lambda_{LIF} = \lambda_0 = 398.289$ nm. The absorption and fluorescence transition are summarized in table 1. As shown in figure 1(a), the fluorescence signal, using the resonant one, has been optimized and the signal to noise ratio has been improved in comparison with measurements carried out in [5]. In the present work, the TD-LIF signal has been amplified, a fact that generates some constraints, such as laser light reflections, for instance, discussed below. Thanks to the resonant fluorescence signal, the AVDFs are measured very accurately with a remarkable reproducibility. The measurements were obtained from a volume of 3 mm^3 above the racetrack (see figure 2). The measured signal corresponds to the axial velocity component (v_z) of the metal particles present in the LIF box (probed volume).

Transition	Ti lines in this work	Ti lines in [5]	Ar ^m
Absorption wavelength (nm)	398.289	398.289	801.699
Absorption transition	$3d^2s^2 (^3F_2)$ $3d^2 (^3F) 4s4p (^1P^o)$	$3d^2s^2 (^3F_2)$ $3d^2 (^3F) 4s4p (^1P^o)$	$3s^23p^5(^2P^o_{3/2})4s$ $3s^23p^5(^2P^o_{3/2})4p$
Fluorescence wavelength (nm)	398.289	736.612	—
Fluorescence transition	$3d^2 (^3F) 4s4p (^1P^o)$ $3d^2s^2 (^3F_2)$	$3d^2 (^3F) 4s4p (^1P^o)$ $3d^3 (^4F) 4s$	— —

Table 1: Ground state transitions of titanium neutral atoms (Ti) and argon metastable (Ar^m) absorption transitions, and their corresponding wavelength in vacuum.

Figure 1(b) shows a typical distribution of Ti neutral sputtered atoms, recorded by TD-LIF and converted in velocity range. One can distinguish two groups of atoms: thermalized (distribution centered at 0 km/s, indexed TH) and energetic atoms (peak at 2.5 km/s, indexed EN). Notice that the measured TD-LIF profile can be affected by the different broadening mechanisms. In our conditions, the most important of them are Doppler, Zeeman, and isotope broadenings. The nearest measurement, close to the target (magnet), was carried out at $z = 1.1$ cm above the racetrack. At this distance, the magnetic field intensity is about 20 mT which causes a Zeeman splitting of 0.1 pm (≈ 200 MHz) [33]. The latter is negligible comparing to Doppler broadening which is in order of 1 pm \simeq 1 km/s for thermalized atoms (see figure 1). The titanium isotopes have a displacement of 0.63 pm (≈ 1.2 GHz) and their abundance is less than 10% [34], for that reason the isotope broadening was also neglected with respect to the Doppler one. As Doppler shift is directly related to the particle velocity (the probed component of velocity is the one along the laser beam), the wavelength has been converted in velocity in figure 1.

Some particularities of these kinds of measurements must be pointed out. The range of wavelengths was limited (9 pm) in order to ensure the diode stability and its longitudinal single mode operation (without jump of mode). At low pressure and close to the target surface, where the sputtered atoms undergo fewer collisions with gas particles, the energetic tail of AVDF is very spread out in velocities. Therefore, that forced us to center the scan domain such as both populations, thermalized (index "TH") and energetic (index "EN") atoms, give a signal on the 9 pm recording range with sufficient intensity. In addition, a fraction of the laser beam is reflected on the target surface, since the laser points towards the target (figure 2(a)). Hence, it diffuses and generates a signal to the left-hand side of the TH distribution (suppressed on the figure 1(b)) which corresponds to a fraction of the signal of the energetic population (symmetrical with respect to the maximum of the TH population). As a result, we did not have access to the base level of the fluorescence signal ($I_{fluo} = 0$), neither on the left-hand side nor on the right-hand side of the scan range. This issue was solved by applying a specific measurement procedure, in two steps, considering that the recorded intensity (I_{mes}) is composed of the fluorescence signal (I_{fluo}) and of the spontaneous plasma emission (I_{pla}) which is a constant, particularly in DC operation. Firstly, by keeping the laser off, the base of the fluorescence (*i.e.*, plasma background emission I_{pla}) signal was determined. Secondly, the pure LIF signal, composed of both, plasma and LIF signal is obtained by removing the plasma emission, $I_{fluo} = I_{mes} - I_{pla}$. This procedure was very helpful for the theoretical fitting of the experimental curves. Regarding TH atoms, the laser reflection affects only their density. Indeed, according to the measured amplitude of EN atoms with negative velocity, the error on the TH density is estimated lower than 10% at $z = 1.1$ cm and it strongly decreases with the distance z .

Figure 3 shows the temperature of the background gas (argon), assuming the same temperature for the ground state of argon and its metastable, for which Doppler broadening was probed by Tuneable Diode-Laser Absorption Spectroscopy (TD-LAS) technique. For a detailed description of TD-LAS experimental setup the reader is referred to Desecures *et al.* [4]. The measurements were performed on the metastable argon state, given in table 1, around $\lambda_0 = 801.69$ nm. To avoid the saturation of the transition, only 1/1000 from the laser power (0.15 mW) was used [35]. The argon temperature is calculated from the full width at half maximum (FWHM) of the Gaussian absorption profile [19], assuming the metastable excited state of argon is in thermal equilibrium with its ground state - the plasma gas. Since the plasma is denser above the racetrack and the gas temperature is measured on the Ar metastable state, one can then assume that the measured Ar temperature represents mainly the gas temperature above the racetrack despite the TD-LAS measurements are integrated along the line-of-sight over the radial direction. Because it is not possible to measure the temperature very close to the target (below $z = 0.8$ mm due to the guard ring), the temperature has been extrapolated by setting $T_{Ar}(z = 0) \simeq 1600$ K at the target surface. This value is coherent with previous measurements of the cathode temperature [19]. Assuming a constant pressure in the discharge chamber, and using the ideal gas law, it comes out that the density of the argon gas is drastically reduced in front of the target, as firstly reported by Rosnagel [36]. The knowledge of the gas density as a function of the distance from the target is found to be a key input parameter for well-fitting the AVDF, as discussed below and in Appendix B. Since the measurement of argon temperature was carried out at 0.4 Pa, the simulation is only performed at this pressure.

2.2 Numerical model

The LPGP (Laboratoire de Physique des Gaz et des Plasmas) has developed over the last two decades several models to describe the magnetron discharge in DC or HiPIMS regime. Among them, OHIPIC is a 2D Particle-In-Cell Monte Carlo Collision (PIC-MCC) model designed to describe the plasma behavior in magnetron discharge in DC or HiPIMS regime. It was successfully used to simulate the plasma behavior in a short pulse operation of HiPIMS discharge [37].

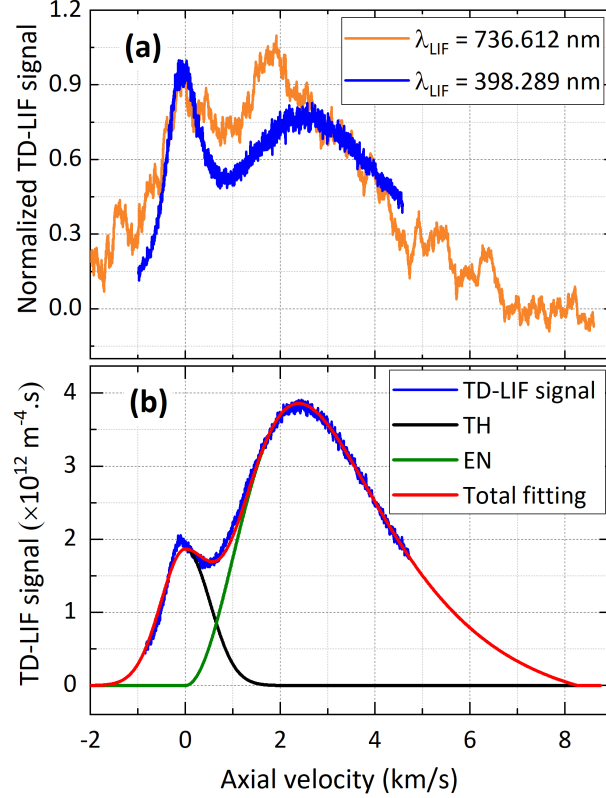


Figure 1: (a) Comparison of the measured TD-LIF signal in this work ($\lambda = 398.289 \text{ nm}$) and in [5] ($\lambda = 36.612 \text{ nm}$). (b) Typical Ti neutral sputtered atoms distribution measured at $z = 1.1 \text{ cm}$, $p = 0.4 \text{ Pa}$, $P = 5 \text{ Wcm}^{-2}$ and with pure Ar gas. The fit used for the two populations (TH for "thermalized" and EN for "energetic") is a Maxwell function for TH atoms and modified Thompson function for EN atoms (equation 2).

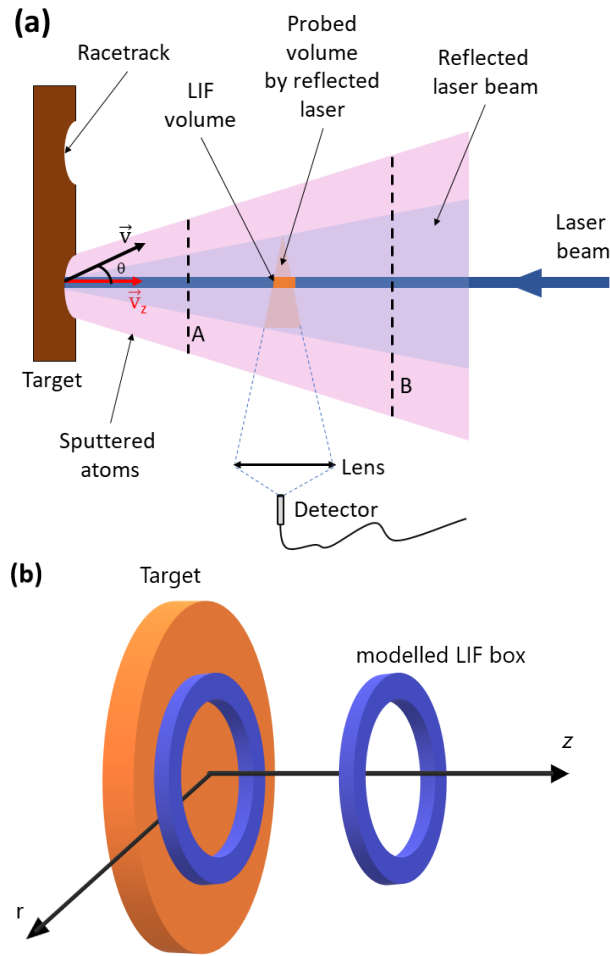


Figure 2: (a) Sketch of the TD-LIF arrangement (in blue) with the laser beam reflection on the target racetrack and the angular dispersion of sputtered atoms (pink), the dashed lines A and B show the dispersion due to the angular distribution of sputtered atoms. Experimental LIF box is also indicated (orange). Only v_z velocity component is probed. (b) Scheme of the modelled LIF box.

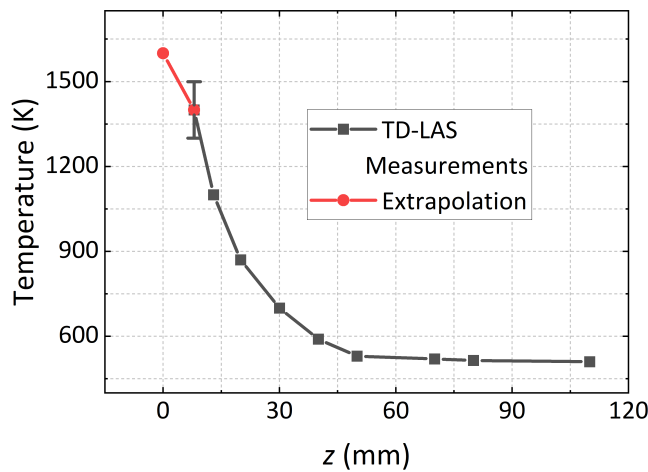


Figure 3: Temperature of the background gas of argon *versus* the distance to the cathode evaluated from the Doppler broadening of Ar^m absorption line at $p = 0.4$ Pa, $P = 5 \text{ Wcm}^{-2}$ and with pure Ar gas. TD-LAS stands for Tuneable Diode - Laser Absorption Spectroscopy.

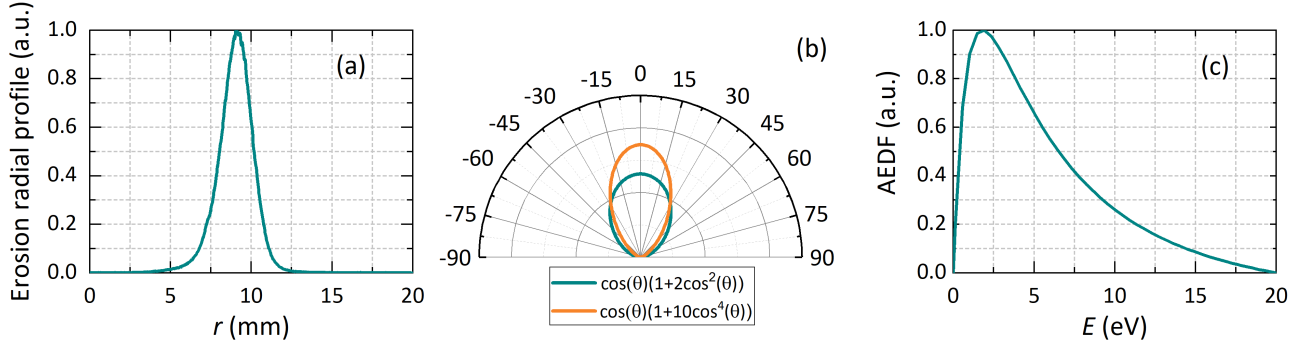


Figure 4: (a) Erosion radial profile of the sputtered titanium due to ion bombardment, the sputtering probability is taken proportional to it. (b) Angle distribution of the sputtered titanium from the cathode surface due to ion bombardment, the distributions have been normalized to 1. (c) Atom Energy Distribution Function (AEDF) of the sputtered titanium from the cathode surface due to ion bombardment.

The OHiPIC model has been used in DC mode to compute the erosion radial profile of the titanium target due to ion bombardment, as shown in figure 4(a). The component of the magnetic field parallel to the cathode is around $r = 9.2$ mm, which defines the location of the maximum erosion of the target, known as the racetrack. A set of three kinetic reactions (ionization of argon, effective excitation of argon - *i.e.* using the sum of all excitation cross sections - and electron-argon elastic scattering) as well as the secondary electron emission due to ion bombardment of the target are included. Details on the used values can be found in [37]. The erosion profile is converted to the radial probability of the target sputtering (called also emission profile of metal atoms), which is used as input in the present Monte Carlo model.

For this work, a modified version of OHiPIC code has been used to only follow the neutral particles sputtered from the target and the collision with the background gas of argon. Hence, many subroutines have been deactivated such as the Poisson's solver, electric field calculation, force interpolation, all essential in PIC algorithm but not required here because there are no charged particles.

The simulation domain is a cylinder (discharge chamber) of 20 mm radius and 50 mm height. $z = 0$ mm corresponds to the target position and $z = 50$ mm to the substrate. Particles are removed when they cross the border of the simulation domain. In addition, the code is parallelized using the domain decomposition method, *i.e.*, each task takes care of a fraction of the entire domain and communicates data to the adjacent sub-domains when needed.

Titanium particles are ejected from the cathode surface ($z = 0$ mm) with the radial coordinate chosen according to the emission profile (erosion radial profile, figure 4(a)) and the initial angle randomly chosen between $-\pi$ and π for a given angular distribution (figure 4(b)). Figure 4(b) shows two different types of angular distributions for the sputtered titanium due to ion bombardment. This angle is measured with respect to z -axis (perpendicular to the cathode). Hence, an angle of 0° corresponds to normal particle ejection from the cathode and it has only an axial velocity component (v_z). Another random angle is taken parallel to the cathode (including r -axis) since Ti atoms are tracked in 3D, *i.e.*, the azimuthal distribution is assumed isotropic. This angle defines the position of v_r with respect to e_x , where \vec{e}_x and \vec{e}_y denote the unit vectors of the cathode plane and \vec{v}_r the velocity component in this plane. Depending on the angular distribution, a particle is more likely to have a higher axial velocity component than equal axial and radial velocity components.

The initial energy is selected according to the modified Thompson Atom Energy Distribution Function (AEDF) shown in figure 4(c) [8]. The equation 2 shows the analytical formulation of this distribution. It is a modified Thompson distribution (equation 1) where E_b is the binding energy of Ti set

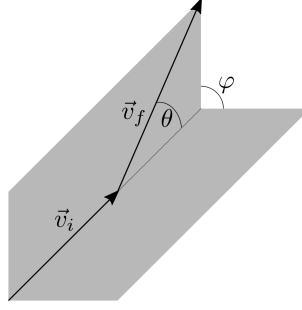


Figure 5: Collision angle in the center of mass. \vec{v}_i denotes the relative velocity before collision, and v_f after.

to 3.3 eV, E_{max} is the cut-off energy set to 20 eV in figure 4(c), s and h two constants set respectively to 0.2 and 1 in accordance to [8, 5]. Moreover, the fitting of TD-LIF measurement near to the target ($z = 1.1$ cm) gives the same parameters since the atoms velocity distribution is only slightly modified by collisions. The influence of E_{max} is small as long as it is above 17 eV as shown in the appendix B.

$$\Phi_T(E) \approx E(E + E_b)^{-3+2s} \quad (1)$$

$$\Phi(E) = \Phi_T(E) \left(1 - \left(\frac{E + E_b}{E_{max} + E_b} \right)^h \right) \quad (2)$$

$$F(\theta, E) = 2\pi \frac{d\sigma}{d\Omega}(\theta, E) \sin \theta \quad (3)$$

$$\begin{aligned} \sigma(E) &= \int_{\varphi=0}^{2\pi} \int_{\theta=0}^{\pi} \frac{d\sigma}{d\Omega}(\theta, E) \sin \theta d\theta d\varphi \\ &= 2\pi \int_{\theta=0}^{\pi} \frac{d\sigma}{d\Omega}(\theta, E) \sin \theta d\theta \end{aligned} \quad (4)$$

Once emitted from the cathode, the trajectories of the sputtered atoms are only subject to the elastic scattering between titanium and argon (see appendix C). The collisions are treated *via* the MCC method coupled to the null collision technique [38] to reduce the computation time. This method requires the density of the background gas, the total cross section values, σ , to compute the collision frequency and the diffusion angles in the center of mass (θ and φ) as defined in figure 5 to compute the post-collision velocity (see below). Here, φ is assumed isotropic, *i.e.*, φ is calculated by generating a random number between 0 and 2π . The other angle, θ , is more critical to accurately model the scattering process and furthermore strongly affects the AVDF. To correctly describe θ and σ , the differential cross section $\frac{d\sigma}{d\Omega}(\theta)$ has been calculated using, as the first guess, the *ab initio* definition of the interaction potential for argon atoms, as proposed by Phelps *et al.* [20]. The details are given in the Appendix A. It has been derived using the WBK (Wentzel, Brillouin, Kramer) approximation allowing the study of a quantum system with a semi-classical approach. Then, the θ distribution can be obtained *via* equation 3 and the total cross section, $\sigma(E)$, from equation 4. The gas pressure is $P = 0.4$ Pa. Hence, the density of the background gas can be calculated from its temperature (see figure 3) using the ideal gas law.

Another possibility to obtain the cross section is to use the M1 model. However, in the M1 model the scattering angle varies linearly with the impact parameter and the inter-atomic potential is in the form of the Born-Mayer formula. The inter-atomic potential from Phelps for Argon is more complex

and has a negative minimum. Furthermore, figure 6 shows that the differential cross section goes through a minimum and so does the scattering angle. In this work, the approximation is only made on the inter-atomic potential.

$$\mu = \frac{m_1 m_2}{m_1 + m_2} \quad (5a)$$

$$\delta_l^{WKB}(E) = \lim_{r_{max} \rightarrow \infty} \left(\int_{r_a}^{r_{max}} \sqrt{2\mu E - \frac{(l + \frac{1}{2})^2}{\rho^2} - 2\mu V(\rho)} d\rho - \int_{r_b}^{r_{max}} \sqrt{2\mu E - \frac{(l + \frac{1}{2})^2}{\rho^2}} d\rho \right) \quad (5b)$$

$$\text{with } r_a \text{ defined as } 2\mu E - \frac{(l + \frac{1}{2})^2}{r_a^2} - 2\mu V(r_a) = 0$$

$$\text{and } r_b \text{ defined as } 2\mu E - \frac{(l + \frac{1}{2})^2}{r_b^2} = 0$$

$$f(\theta) = \frac{1}{2i\sqrt{2\mu E}} \sum_{l=0}^{\infty} (2l + 1)(e^{2i\delta_l(E)} - 1)P_l(\cos\theta) \quad (5c)$$

where P_l denotes the Legendre polynomials

To calculate the differential cross section of the scattering between titanium and argon, corresponding to a hetero-nuclear interaction, the set of equations 5a to 5c combined with equation 6a should be used. *A contrario*, for homo-nuclear interaction, equations 5a to 5c and 6b should be considered instead. However, using either equation 6a or 6b does not produce satisfactory results when comparing AVDF from the TD-LIF measurements and the model (see Appendix B). Instead, a slightly modified formulae has been applied (equation 6c) where a γ factor has been added. The best match between the model and measured AVDF has been found for $\gamma = 1.5$. The corresponding differential cross section is shown in figure 6(a) for three values of energy. Figure 6(b) shows the total cross section as a function of the energy.

$$\frac{d\sigma}{d\Omega}(\theta) = |f(\theta)|^2 \quad (6a)$$

$$\frac{d\sigma}{d\Omega}(\theta) = |f(\theta) + f(\pi - \theta)|^2 \quad (6b)$$

$$\frac{d\sigma}{d\Omega}(\theta) = \gamma |f(\theta)|^2 \quad (6c)$$

Once the diffusion angle is known, the algorithm from [39] can be applied (equations 7 to 9). \vec{v}_A^i and \vec{v}_B^i are the initial velocities of the particles A and B, respectively, before collision, while \vec{v}_A^f and \vec{v}_B^f their final velocities after collision. Applying equations 7, 8, and 9, one obtains the velocity components after collision with $g = \|\vec{g}\|$.

$$\vec{g} = \vec{v}_B^i - \vec{v}_A^i \quad (7)$$

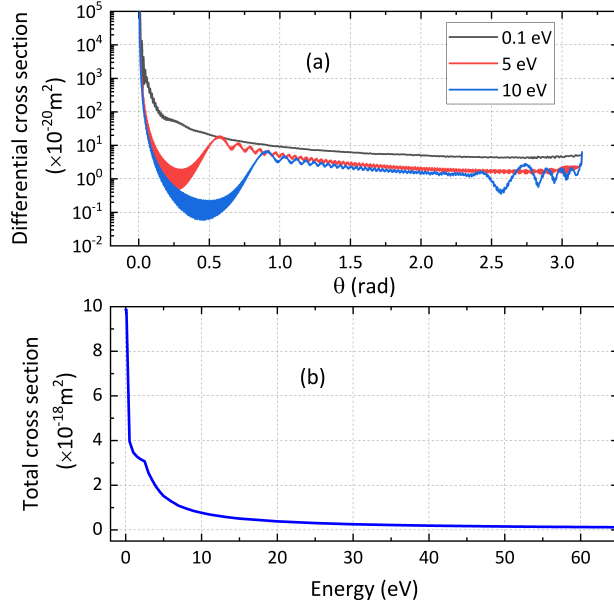


Figure 6: Calculated cross sections of elastic collision between Ti and Ar for $\gamma = 1.5$ using the set of equations 6. Panel a) shows the differential cross section versus the angle and panel b) shows the total cross section *versus* the energy in the center of mass.

$$k_x = \cos \frac{\theta}{2} \sqrt{1 - \frac{g_x^2}{g^2}} \cos \varphi \quad (8a)$$

$$k_y = -\cos \frac{\theta}{2} \left(\frac{g_y g_x \cos \varphi + g g_z \sin \varphi}{g \sqrt{g^2 - g_x^2}} \right) \quad (8b)$$

$$k_z = -\cos \frac{\theta}{2} \left(\frac{g_z g_x \cos \varphi - g g_y \sin \varphi}{g \sqrt{g^2 - g_x^2}} \right) \quad (8c)$$

$$\vec{v}_A^f - \vec{v}_A^i = \frac{2m_B}{m_A + m_B} \sin \frac{\theta}{2} \left(\vec{g} \sin \frac{\theta}{2} + g \vec{k} \right) \quad (9a)$$

$$\vec{v}_B^f - \vec{v}_B^i = \frac{-2m_A}{m_A + m_B} \sin \frac{\theta}{2} \left(\vec{g} \sin \frac{\theta}{2} + g \vec{k} \right) \quad (9b)$$

At every few iterations (typically 100 corresponding to a real flight time of 1 ns), the code checks if the position of the particle is within a 'LIF-box', corresponding to the main probed volume (see figure 2(a)). Their geometry represent circular volume with rectangular section of 3 mm in width and 1 mm in height, surrounding the entire magnetron, *i.e.* 2π , and located above the race-track ($r \approx 9.2$ mm) as shown in figure 2(b). LIF-boxes have been placed at every millimeter from the target. If a particle is inside one of these, then it is added to the calculated AVDF. Doing the average of the AVDF over one million iterations allows for an improved statistic. The AVDFs can also be sorted by the number of collisions a particle underwent because the code allows to track this number throughout the simulation, *i.e.*, the obtained AVDF for each population performing the same number of collisions with the buffer gas has been analyzed (section 5, figure 11).

3 Model calibration procedure

The aim of the present work is, as stated, to compare the AVDF obtained by TD-LIF measurements and by the MCC model of the sputtered Ti transport in DC regime. Because the ionization ratio of the sputtered atoms of titanium is low ($< 1\%$) in DC [40], the ionization of titanium is neglected. Thus, the plasma does not affect the titanium trajectories and it is therefore neglected. Only the radial emission profile (figure 4(a)) was calculated self-consistently, *i.e.*, with the plasma taken into account *via* the PIC algorithm using OHiPIC model.

As said before, OMEGA model [5] has already been used to fit the AVDFs obtained by TD-LIF measurements [19]. The former measurements obtained at a different wavelength ($\lambda_{LIF} = 736.612$ nm, see table 1) are depicted in figure 1(a) and one can clearly see the huge improvement of the TD-LIF signal with the new experimental arrangement used in this work ($\lambda_{LIF} = 398.289$ nm, table 1). Indeed, the procedure to remove the background (plasma emission) and the better adjustment of the diode laser led to a more accurate description of the two populations composing the titanium sputtered vapor. Particularly, the thermalized distribution is very sensitive to the interaction cross section. Precisely, this part of the signal was very noisy in the early measurements [19]. Furthermore, the AVDF obtained by the model using the Ar-Ar interaction cross section proposed by [5] does not match well the AVDF carefully recorded in this work.

Reproducing numerically the TD-LIF measurement of sputtered Ti AVDFs for different discharge conditions is not an easy task. However, we took advantage here of having a much better quality of the recorded signal, and hence the model could also be improved. As said, the radial emission profile of sputtered atoms (figure 4(a)) is predicted by OHiPIC, but a lot of input parameters could drastically affect the simulated AVDFs, as shown in Appendix B. In fact, the sputtered atoms have an angular distribution that depends on the geometric state of the target state (racetrack) and the impinging energy of the plasma ions (figure 4(b)). Also, they spread up to a maximal energy (the cutoff energy of modified Thompson's formula) (figure 4(c)). The cutoff energy is mostly a function of the ion energy and only weakly depends on the target material [41]. As the DC operation voltage is 300V and based on our TD-LIF measurement, it was taken below 10% (cut-off energy of 20 eV) of the impinging energy of ions, which is about 300 eV for a collisionless sheath. In addition, another parameter - the interaction collision cross section Ti-Ar - is not known. Here, we propose another cross section, based on *ab initio* definition of the inter-atomic potential, as suggested by Phelps *et al.* [20]. In the following, we show the most suitable combination of those parameters which generates the best fit of the experimental measurements.

The figure 7 shows the AVDF from the measurements and from the model for two positions from the cathode, $z = 11$ mm and $z = 20$ mm. The TD-LIF signal is shown in blue and its corresponding fit is in red. The results obtained by the model are represented in green. In both cases, the AVDFs have been normalized so that their integrals are the same. The AVDFs from the model and experiment are in close agreement. The energetic population relaxes to a thermalized one, as expected, by the theory and by the measurements. However, the transition between the energetic part and the thermalized one is not in perfect agreement. This is mainly due to the cross section not being accurate enough. Appendix B shows a study of different parameters on the AVDFs such as the cross section, the angular distribution, and the value of E_{max} from the modified Thompson and their direct impact on the calculated AVDF. Although the curves do not match perfectly, the results shown in figure 7 are as close as possible, so far. One would need to know the exact inter-atomic potential between Argon and Titanium to go further.

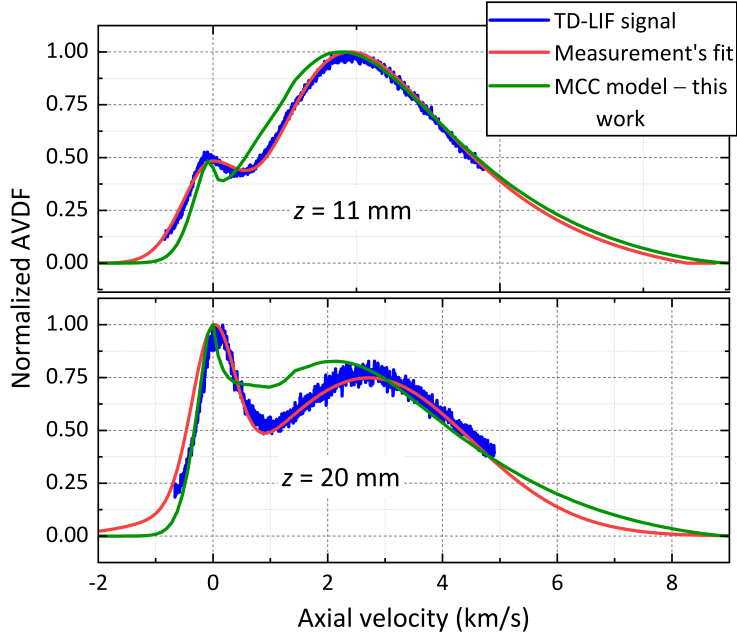


Figure 7: Velocity distribution function of the sputtered atoms (AVDF) of titanium for the cases listed in table 2 (Appendix B) for two distances from the cathode. Blue lines show the measurement, red line the fit of the measurement and green line the MCC model results. Note that all velocity distribution functions (experimental and given by the present model) have been re-normalized for their easier comparison.

4 Results

4.1 Collisions effect on sputtered titanium AVDF

As it was mentioned before, in section 2.1, AVDFs of sputtered atoms are mainly affected by the Doppler shift, all other broadening contributions being negligible. Then, the measured LIF emission profile is due to the distribution of the probed atoms having at least one velocity component along the laser beam. Hence, the closer the light of sights to the target, the more energetic atoms are recorded since there are very few or no collisions between the sputtered atoms and the background gas. Consequently, the TD-LIF signal of the energetic atoms (EN) should be fitted by the modified Thompson function (see figure 1(b)) [8]. The records got for other positions, far away from the target, present the signature of a cooling phenomenon of these energetic atoms during their transport between the target and the probed volume, since they undergo collisions with the background gas. They transfer a part of their energy to the heavy species of plasma (neutral and ions in ground state or excited). In addition, these collisions affect their direction which provokes a variation in their velocity distribution. Therefore, these processes could modify the tail of sputtered AVDF, especially for Ti atoms for which the mass is close to the mass of Ar, the background gas. Obviously, the higher the number of collisions of metal atoms with the gas, the closer the velocity component distribution to a Maxwell function. So, increasing the pressure will help the thermalization as it is the case far from the target.

Among the advantages of the MCC model developed herein, one is the track of the number of collisions that Ti sputtered particles underwent during their transport. Figure 8 shows the model results at different distances from the target and at low pressure (0.4 Pa), the most interesting since the thermalization takes much longer. For each class of velocities, the sputtered particles have been sorted according to the number of associated collisions. As expected, close to the target ($z = 5$ mm),

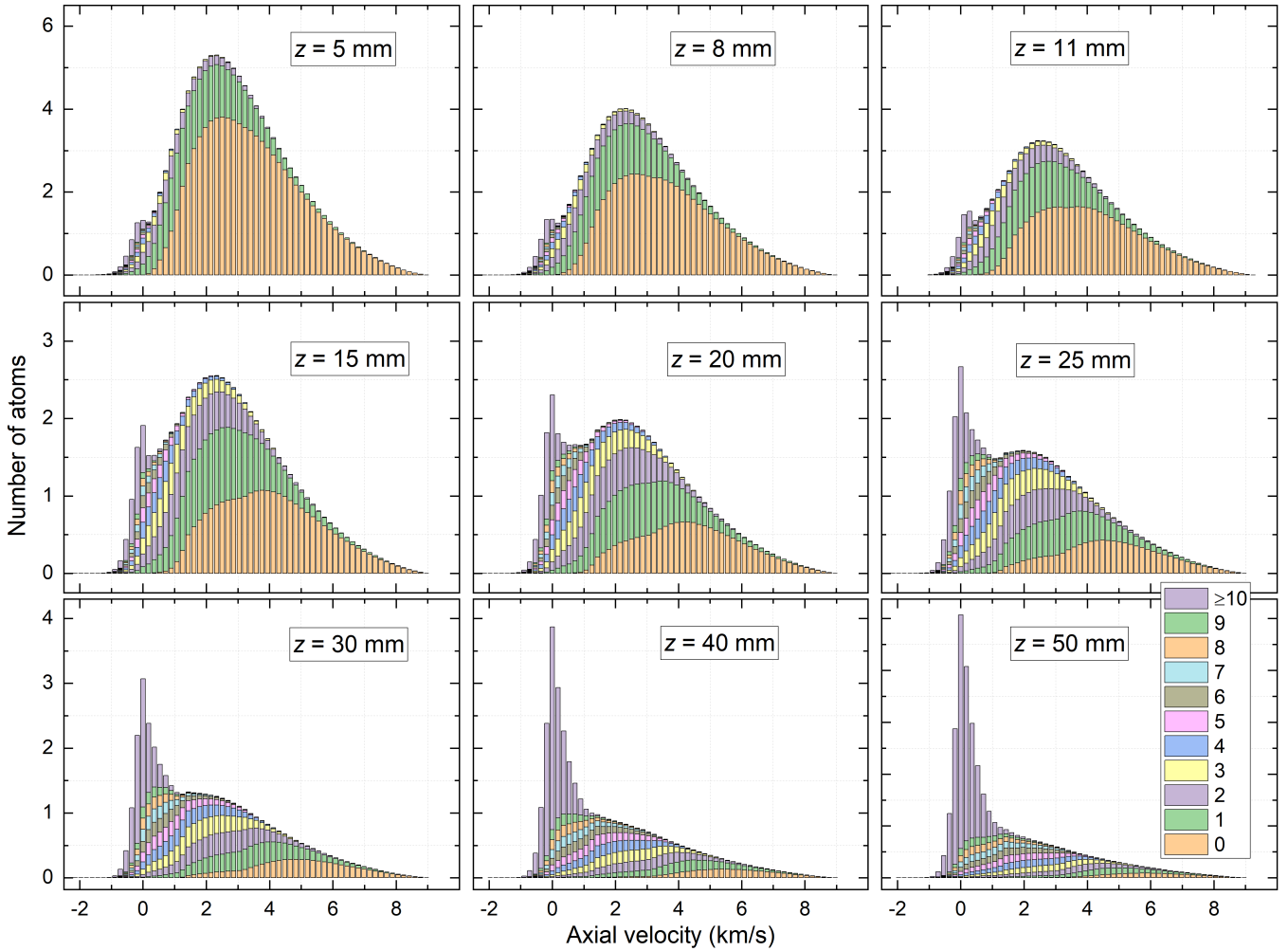


Figure 8: Simulated AVDFs of Ti sputtered atoms in which the number of collisions is shown by a stacked column at different distances from the target, $p = 0.4$ Pa and $P = 1.5$ Wcm⁻².

the AVDF is dominated by the particles which have never interacted with the Ar gas, called ballistic atoms (yellow bars on the figure). By increasing the distance z , the fraction of ballistic atoms, traveling without collisions, becomes lower and lower compared to the atoms performing one or more collisions. At $z = 20$ mm, most of the atoms, which have undergone collisions, have an axial velocity lower than 5 km/s. Note that at this distance ($z = 20$ mm) the fit of the measured EN atoms by Gauss function is better than modified Thompson function.

For $z = 11$ mm, one can see that about half of the particles are still ballistic, while the other half underwent one (about 25%) or several collisions. The thermal population is already visible, but let us notice that it corresponds to particles that have undergone 10 or more collisions, some much further from the target and crossing again this particular LIF box. Also, it is remarkable the presence of particles with negative velocities very close to the target ($z = 5$ mm). They represent a small fraction of the total sputtered atoms returning back to the cathode, but also after an important amount of collisions, feeding a back-stream of scattered atoms, discussed more in detail in section 5. The amazing result is the last frame of figure 8, recorded for $z = 50$ mm, where almost all the particles after 5 collisions still keep a positive axial component of the velocity. After 6 collisions or more they start to feed the negative velocity wing of the distribution, but the fully thermalized particles require at least 10 collisions, as found closer to the target.

4.2 Gas rarefaction in DC magnetron sputtering

In spite of the unexpected effect of collisions relatively close to the target ($z = 20$ mm) leading to a relaxation of energetic atoms, it cannot explain the experimental result reported in figure 3. Indeed, the argon gas is very hot close to the target ($z < 10$ mm), region dominated by the ballistic Ti atoms. The so-called 'wind effect', *i.e.*, the momentum transfer from the sputtered metal to the gas, is far to be sufficient. This effect was found important in HiPIMS discharges [23, 42], but for the surface current density on the target in DC mode, it is not dominant. Indeed, assuming that half of the impinging Ar^+ contribute to the flux of hot Ar (denoted Ar^{H}) reflected on the target [43], $\Gamma_{\text{Ar}^{\text{H}}}$, the flux of sputtered metal, Γ_{Ti} , is found to be lower than the flux of hot Ar ($\Gamma_{\text{Ar}^{\text{H}}} = 0.5\Gamma_{\text{Ar}^+}$ and $\Gamma_{\text{Ti}} = Y\Gamma_{\text{Ar}^+}$ leads to $\Gamma_{\text{Ar}^{\text{H}}}/\Gamma_{\text{Ti}} = 0.5/Y > 1$, see Appendix C). Since their energy is higher, the momentum transferred to the neutral buffer gas of Ar dominates with respect to the momentum transferred by the sputtered metal. In his pioneering work, Rossnagel [36] pointed out the metal sputtering wind as the main effect for the pressure decrease in front of the target, especially in the ionization region. However, he also mentioned other possible origins for this rarefaction such as the back-scattering of energetic ions (neutralized in contact with the target) or energetic gas neutrals produced by charge transfers from the energetic ions accelerated towards the target. Many of them rebound on the target and feed the so-called 'warm' atom population. This is clearly a valuable route to explain such a high temperature of argon just in front of the target. Indeed, Ar^+ ions hit the target with about 200 eV, and they can bounce on the target joining the gas phase as very energetic neutrals. This population of energetic argon atoms was very well described in the HiPIMS mode by Huo *et al.* [43]. In addition to this energetic neutral argon (so-called 'Hot') produced at the target surface, another Ar population was considered in [43]. This second population originates from Ar^+ ions recombining and superficially penetrating the target (subplantation) leading to a small concentration of the noble gas in the outermost part of the target (one to several monolayers). So, they leave the surface, sometimes spending a while on/in the target or being desorbed from the sublayer during the sputtering process. These 'warm' atoms (Ar^{W}) are characterized by an energy much lower than the back-scattered group (Ar^{H}), but still significantly higher than the equilibrium temperature of the background gas far from the target. Ar^{W} is assumed to leave the cathode in equilibrium, at the local target temperature. It is worth mentioning the strong disagreement found in the present work between the MCC simulation and the TD-LIF measurements of the AVDF (see appendix B, case 3), if the temperature axial profile in the ionization region is ignored, *i.e.*, if the argon gas density is taken constant in the whole discharge volume. Therefore, the rarefaction effect is certainly present in all types of magnetron discharges, but in DC mode Ar^+ plays the main role. This rarefaction effect contributes also to the ballistic transport of sputtered species in front of the target by the local decrease of the gas (Ar) density.

5 Discussion on the metal transport in intermediate pressure regime

The knowledge of the metal transport regime is key information for all the deposition techniques, and it is particularly delicate to evaluate for magnetron discharges. Indeed, at high pressure (> 1 Pa), the mean free path decreases (< 5 mm) and the sputtered species thermalize relatively fast. However, at intermediate pressures ($0.1 < p < 1$ Pa), the thermalization process is not obvious even if it is often assumed. In this range, the heavy (metal) particles ejected from the target behave as a directed flux ($v_z > 0$) and they slow down and further thermalize through interactions with the buffer gas. However, for such low pressures, often, the full thermalization is not achieved, and this is the focus here. As expected, at very low pressures (< 0.05 Pa) the transport becomes dominant ballistic, but the discharge

(at least the magnetron discharge) cannot operate.

TD-LIF measurements have been carried out for five different distances ($z = 11, 20, 30, 50,$ and 80 mm), above the racetrack where Ti atoms are mainly sputtered, and for two different discharge pressures ($p = 0.4$ and 1.3 Pa, typical intermediate pressure and high pressure, respectively). These measurements with the corresponding fitting are shown in figure 9. Even at the intermediate pressure, always far from the target at $z = 80$ mm, the EN atoms almost disappear and the vapor is quasi-thermalized, as expected. The absolute measurements performed by TD-LIF give access to the particles density,

$$[Ti]_X = \int_{-\infty}^{+\infty} AVDF_X dv_z \quad (10)$$

the flux towards the substrate ($v_z > 0$),

$$\Phi_X = \int_0^{+\infty} v_z AVDF_X dv_z \quad (11)$$

and energy distribution where X represents the population, respectively TH or EN. Figure 10(a) shows the axial dependency of the flux for both populations of atoms. The EN atoms which have undergone none or very few collisions (quasi-ballistic transport) travel confined in the emission cone (see figure 4(b)). As they move away from the target, they spread out as the cone volume (figure 2(a)) increases [31], depending on the perpendicular velocity component with respect to the axial one. Hence they can advance simultaneously, at the same 'z' location, but drifting out of the experimental LIF box, and so they are excluded from the probed volume further and further from the target. In the ionization region (up to at least $z \leq 30$ mm, where the electrons are trapped) and for the two pressures, this angular expansion phenomenon explains the continuous decay of the EN flux, since this loss is not found, in terms of gain, on the TH population. Consequently, the EN density decreases as well, the dispersion of the EN atoms far from the racetrack clearly leads to their dilution (fewer atoms per volume unit). However, by comparing the flux of EN atoms at 0.4 Pa and 1.3 Pa, we notice a decrease at $z = 11$ mm by a factor of 1.5 when the pressure increases by a factor of 3 . In our conditions, the pressure does not significantly affect the amount of sputtered atoms because the measurements were performed at constant discharge power $P_{DC} = 5 \text{ Wcm}^{-2}$. Then, even if the discharge voltage and the discharge current slightly vary with pressure, the number of sputtered atoms is mainly imposed by the power discharge. Let us remark that the voltage increases a few tens of Volts by changing the pressure from 1.3 Pa to 0.4 Pa, so the ion current is slightly lower to preserve the power density constant. In other words, the sputtered flux of particles (source term) is slightly lower at low pressure. But, considering the gas rarefaction reported and discussed in section 4.2, it is more important at 0.4 Pa (figure 3) than at 1.3 Pa, and this can partly be at the origin of the observed flux decrease of energetic sputtered atoms. This proves that the effect of one or two collisions (loss of energy and direction change) is already clearly visible very close to the target at 1.3 Pa (mean free path of approximately 5 mm). So, even if the source term is larger at higher pressure, the change in the transport regime from quasi-ballistic to diffusive inverses the metal fluxes very close to the target. For the sake of comparison with the MCC results, only the qualitative comparisons will be made for the velocity distribution, and numerical curves are renormalized to the unit.

TH atoms are the result of the cooling down of EN atoms undergoing collisions with the buffer gas. However, the question is still open - how many collisions are necessary for these particles to be in full thermodynamic equilibrium, *i.e.*, the same distribution on the three components of the velocity in velocity space. As previously mentioned, the number of EN atoms decreases as a function of the distance z and it should feed the TH group of atoms when the distance from the target increases (figure 9). Once thermalized, these atoms equally travel in all space directions, and independent of the flight

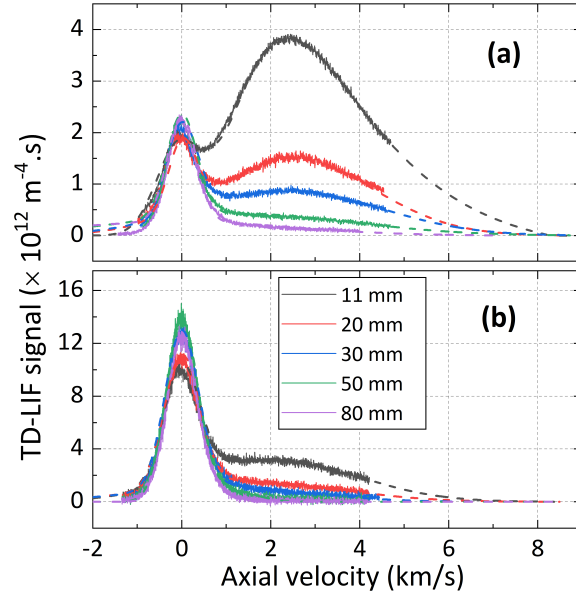


Figure 9: Measured AVDFs of Titanium sputtered atoms at $p = 0.4$ Pa (a) and 1.3 Pa (b), $P_{DC} = 5 \text{ Wcm}^{-2}$ and for different distances z . The dashed lines are Maxwell fit for TH and Gauss or modified Thompson fit

for EN.

time (as it is the case in DC), they enter all LIF boxes by diffusion. The relaxation of EN atoms from modified Thompson to Gaussian function allowed for a better description of EN atoms. The variation of the flux of TH atoms with z and pressure (at 0.4 Pa and 1.3 Pa) follows the variations of the flux of EN atoms at 0.4 Pa whereas at 1.3 Pa the flux of TH atoms seems constant as function of the distance z (figure 10(a)). The variation of TH atoms density is shown in figure 10(b). A slow decrease with the distance z can be observed on the density at low pressure (0.4 Pa), but at 1.3 Pa an opposite trend is observed up to $z = 50$ mm and it decreases beyond. Because of the lower thermalization at 0.4 Pa the behavior of the density and the flux toward the substrate of TH atoms could be explained by the decrease of the source generating the TH atoms, *i.e.* the dilution of EN atoms density is induced by the angular distribution of sputtered atoms (figure 2(a)). At 1.3 Pa, the thermalization is important and it seems to compensate for the decrease due to the angular distribution of sputtered atoms, so the flux is constant. The axial dependency of the density reflects the full thermalization of sputtered atoms occurring at $z \sim 50$ mm. So, from this position, the density decreases in all space directions due to diffusion. As expected, the temperature of TH atoms shows a gradient as function of distance z (figure 10(c)) and the cooling of the TH atoms is more efficient at 1.3 Pa compared to 0.4 Pa. At 0.4 Pa the temperature of TH atoms seems very close to argon temperature measured by TD-LAS (figure 3), a difference of about 250 K is registered close to the target ($z < 30$ mm) while it is within 100 K interval with respect to argon temperature far from the target ($z > 30$ mm). These discrepancies can have different origins, but the main two are the measurement and the fit. The uncertainty of the latter one seems dominant. However, remember that the gas temperature T_{Ar} was measured on metastable species and assumed the same for the gas ground state. Moreover, Ar-Ar collision is much more effective for thermalizing the gas (homo-atoms) while Ar-Ti collision frequency is more anisotropic, and hence tends to preserve the forward velocity. Therefore the thermalization process of sputtered atoms is longer and this could explain that Ti temperature is slightly higher than Ar one, especially close to the target. Overall, the temperatures of the two species (Ar and Ti) are close enough to suggest that TH atoms and the background gas are in local thermal equilibrium whatever the distance from the target is (within the margin of the error bars).

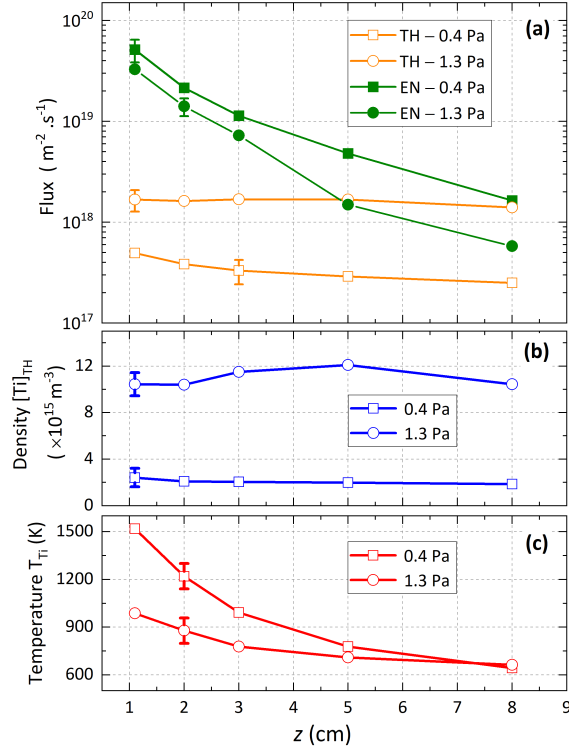


Figure 10: (a) Flux of EN and TH atoms *versus* the distance z . (b) Density and (c) temperature of TH atoms *versus* the distance z .

After the analysis of the experimental results, the MCC model brings new microscopic insights on the thermalization and the transport of sputtered metal in the intermediate pressure regime. Figure 11 well illustrates the role played by the metal-gas kinetics when moving away from the target, at 0.4 Pa. This is another way to represent the information contained in figure 8. The first line of the matrix of panels composing this figure corresponds to AVDFs at different distances z indicated on the top of each column. The bold label in each panel represents the loss due, at least, to angular distribution (*i.e.* 'dilution' of metal atoms moving away from the target) as a function of the distance z . It was calculated by the following relationship: $R_1 = N_z/N_{z=1 \text{ mm}}$, where N_z denotes the number of atoms in a numerical LIF box located at the distance z and $N_{z=1 \text{ mm}}$ the number of atoms in the numerical LIF box centered at $z = 1 \text{ mm}$ (initial number of particles leaving the target, in the model). This matrix (figure 11) can be further read by columns or by rows. For each location z , the columns show the local decomposition of the AVDF grouping the metal atoms by the number of collisions that occurred from the target to this distance and contained in the numerical LIF box. The rows correspond to the growing number of collisions undergone, indicated on the left-hand side. Therefore, the line marked "0" represents the AVDF of the ballistic particles, at different distances from the target. The following rows show the distribution of the particles which collided once, twice, and so on, up to "11" collisions. Each panel has inside a label indicating the percentage of sputtered atoms ($R_2 = N_n/N_z$) that underwent "n" collisions (N_n being the number of atoms that collided "n" times) from total sputtered atoms in the LIF box located at the distance z .

Another ratio has been calculated: $R_3 = \langle v_n \rangle / 2v_{th}$ where $\langle v_n \rangle$ denotes the average velocity of atoms evaluated from the AVDF, whatever its form is, corresponding to the atoms that underwent "n" collisions. For the EN group of atoms, $\langle v_n \rangle$ represents the group velocity. $v_{th} = \sqrt{\frac{kT}{m_{Ti}}}$ is the thermal

velocity of thermalized atoms calculated *via* gas temperature (figure 3). This ratio was used to distinguish different regimes of transport. Hence, when $R_3 > 1$ the transport is considered forward flux (panels filled in blue), being highly dominated by particles moving forward (positive group velocity). When $R_3 < 1$ the transport is considered diffusive and the atoms are mainly thermalized or very close to reaching the thermal equilibrium (panels filled in beige and wheat). However, a fraction of thermalized atoms has a dominant negative group velocity leading to a "back-stream" of atoms towards the target. We deliberately chose to mark $R_3 < -0.4$ to evidence this population of atoms returning back to the cathode due to the diffusion stream, as explained before (wheat color).

This color code makes easily distinguishable the different transport regimes that coexist in the total AVDF (first row of figure 11). The information contained in this figure is explained through a few examples. Let us discuss, for instance, the velocity distribution of particles about 20 mm away from the target. The number of atoms performing a free path is 28 % of the total number at this distance, which is consistent with the result of classical formulae of collision probability ($\exp(\frac{-z}{\lambda})$) when a mean cross section of 2.10^{-18} m^2 (see figure 6) is used to determine the mean free path ($\lambda_{0.4 \text{ Pa}} \approx 15 \text{ mm}$ at 1250 K). The thermalization can occur only after, at least, 7 collisions at 0.4 Pa and the fraction of thermalized particles represents less than 9%, *i.e.*, at this distance, most of the particles preserve their forward motion, even if they interact seven times with the gas atoms. This is also exposed in figure 8. For $z = 5 \text{ mm}$, almost all the particles compose the forward flux (96.7 %) and only 0.57 % of them get thermalized after about four collisions. For $z = 30 \text{ mm}$, 81.7% of the particles are contribution to the forward flux (9% less than at $z = 20 \text{ mm}$), and they do not get thermalized even after 9 collisions (last column in blue). This phenomenon is counter-intuitive. Indeed, the number of particles composing the forward flux group decreases with z (at $z = 30 \text{ mm}$ it represents only 20% of the total sputtered particles, bold label - R_1 - row 1), this ballistic group is composed of the more energetic particles as well (row 1, last panel). Hence, their thermalization requires more and more collisions. Remember that the AVDF is plotted here only for the v_z component of the velocity. So, the slow particles ejected from the target have a much higher chance to interact with the gas, even in the very few millimeters in front of the target. Consequently, their large majority are scattered out of the LIF box, and they are not accounted anymore in the next z locations. This is why the first dimensionless number R_1 decreases with z (bold number in the first row). Hence, the farther is probed the sputtered population, the most it is dominated by energetic particles. This can be undoubtedly seen in the row labeled "0". With increasing z , the mean energy of atoms having positive group velocity increases as well, and therefore more and more collisions are required to thermalize this fraction of energetic atoms surviving far from the target.

Another important piece of information contained in figure 11 concerns the flux of atoms returning back to the target. First, there are only a few of them ($< 1\%$) at $z = 1 \text{ mm}$, for instance, and all of them, independent of the position, have negative mean velocities, but it is close to zero. They mainly originate from the location where the majority of the sputtered atoms are fully thermalized and starting with this point the diffusion brings, roughly, half of the atoms back to the cathode while the other half diffuses towards the substrate. At $p = 0.4 \text{ Pa}$ neither the MCC model nor TD-LIF measurement can be used to determine the distance of the full thermalization because of the high mean free path ($\lambda_{0.4 \text{ Pa}} \approx 15 \text{ mm}$) and the decrease of the source generating TH atoms due to the angular distribution of sputtered atoms. However one can rely on TD-LIF measurement to determine this distance at $p = 1.3 \text{ Pa}$, it corresponds to distance z where the density of TH atoms get the maximum, figure 10(b) indicates that at $z \approx 50 \text{ mm}$ the sputtered atoms are fully thermalized.

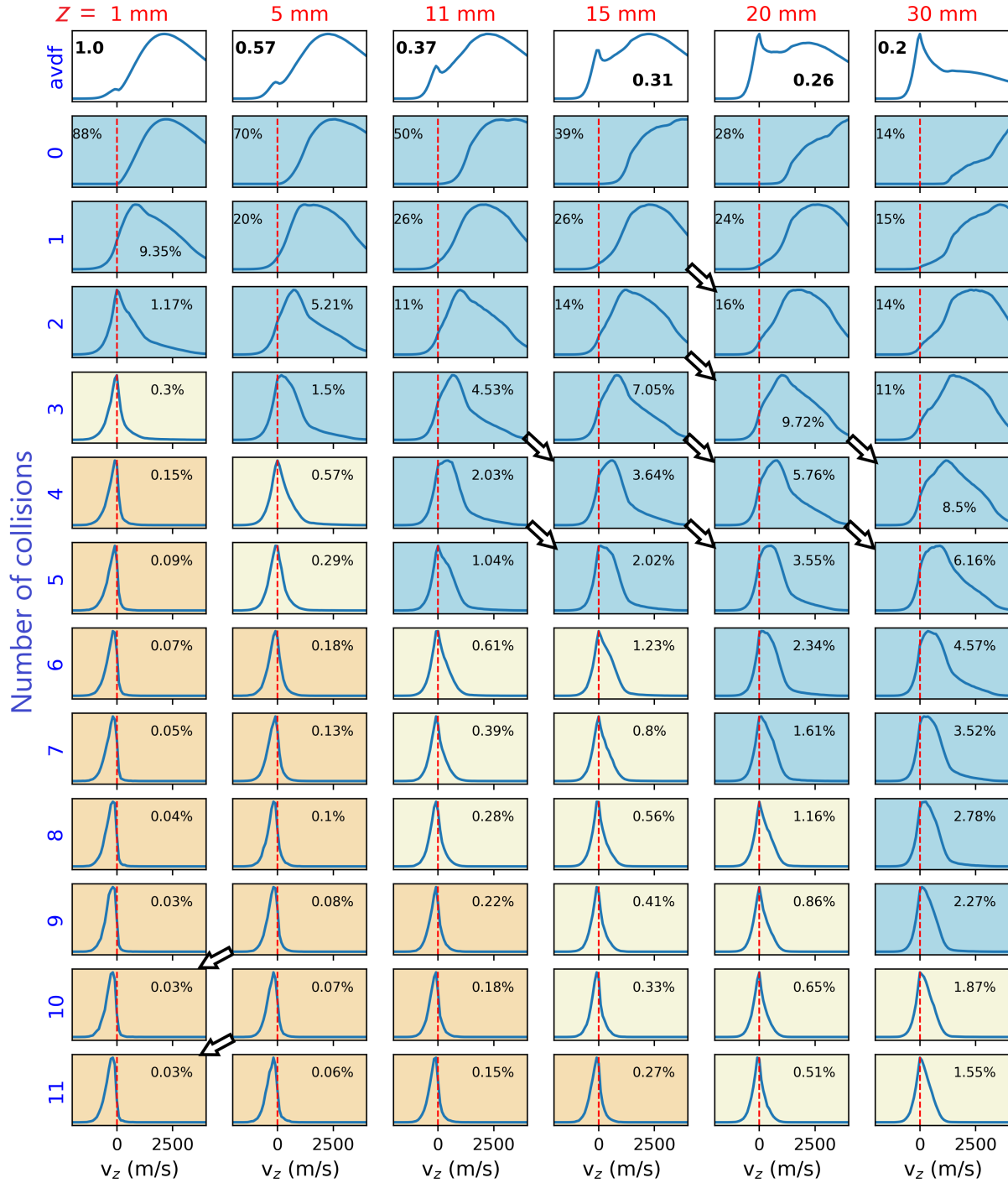


Figure 11: Top 5 figures are the simulated AVDFs *versus* the distance from the target at $p = 0.4 \text{ Pa}$, $P = 1.5 \text{ Wcm}^{-2}$. The bold label in the first row of panels corresponds to the ratio of number of atoms at distance z to the number of atoms at distance $z = 1 \text{ mm}$ ($R_1 = N_z/N_{z=1 \text{ mm}}$). The colored panels represent a matrix where the columns and rows correspond respectively to a distance from the target and the velocity distributions of the group of sputtered particle atoms that underwent the same number of collisions with the gas. For each column, constant z , the fraction of particles undergoing "n" collisions from the total number of particles at z is indicated as label ($R_2 = N_n/N_z$). For more information see the text. Two regimes of transport are distinguished on the matrix; blue figures mark the forward moving metal, corresponding to energetic particle, beige and wheat figures are related to the diffusive transport, but the latter indicates the back-streaming transport (*i.e.*, atoms returning back to the target). The black arrows on figure indicate from where the atoms mainly come. All the distributions are re-normalized to the unit for the sake of clarity.

6 Summary conclusions

The transport and the thermalization of neutral Ti sputtered atoms in the intermediate pressure regime has been studied combining TD-LiF measurements and MCC simulation for a DC magnetron discharge in argon. Using a resonant LIF signal and taking advantage of the high resolution of this technique (space and spectral), these measurements allowed to accurately describe the neutral Ti atoms velocity distribution function (AVDF). Because the transport and the thermalization of sputtered atoms are strongly affected by the gas rarefaction in magnetron sputtering process the gas temperature has been measured with tunable diode laser absorption technique and it was used as input alongside the measured Ti AVDFs as output to calibrate the MC model. Several calculation, combining various input parameters (the angular distribution of sputtered atoms, the Ti AVDFs at the target surface, and the Ti-Ar cross section) were performed and the best agreement of modeled and measured AVDFs was reported. The hetero-nuclear Ti-Ar collision cross section based on the *ab initio* formulae of the interaction potential derived from the homo-nuclear Ar-Ar collision was crucial to reproduce the experiments as well as the neutral gas temperature profile in front of the target. Even if the discharge was operated in DC, the gas rarefaction is important mainly due to the warm argon atoms released from the target. In addition, a revisited analytical formulation for Ti-Ar scattering cross section is proposed. Improved measurement and modeling compared to the previous works allow a better separation of thermalized and energetic atoms and a better understanding of the metal-gas transport.

The Monte Carlo Collision model developed here follows the sputtered atoms and accounts for the number of collisions with the background gas they underwent in 3D. The effect of gas pressure on the energetic atoms population was studied, the results show that energetic atoms relaxes from a modified Thompson to Maxwell velocity distribution function at 20 mm within the target for 0.4 Pa and 11 mm for 1.3 Pa. This result was confronted to the modeled AVDFs and it was confirmed that relaxation is mainly due to collisions with gas particles: the relaxation occurs when $> 50\%$ of energetic (EN) atoms underwent at least one collision. A global image was given on Ti AVDFs as a function of the number of collisions and the distance from the target to evidence the ballistic, forward oriented, and diffusive transport. The thermalization and the transport of the sputtered beam were discussed considering the complexity of the gas species transport in the intermediate pressure regime, where neither the ballistic nor the diffusion equations cannot be used. A part of diffusive transport corresponding to the back-streaming transport of sputtered atoms towards the target was highlighted. In the case of DC magnetron studied here the atoms back-stream to the target represents less than 2% of the sputtered metal. They originate from the location of the fully thermalized species, which obviously get closer to the target with the increasing pressure. For low pressure (0.4 Pa), this distance is estimated at $z = 40$ mm, exceeding two mean free paths (mfp). However, that does not mean the atoms have to exhibit 2-3 collisions to thermalize, as often concluded in the literature (by simply dividing this distance by the mfp), but much more to fully thermalize the ballistic fraction of atoms. The fraction of thermalized atoms has been also estimated as well as the fluxes of the two groups (populations) of atoms, namely thermal and energetic.

The outlook of this work is the simulation of the ionization of metallic species in HiPIMS discharge where a significant decrease in the deposition rate was reported because of the back attraction of ionized species.

Acknowledgments

This work was granted access to the HPC resources of CINES under the allocation 2018-A0040510381 made by GENCI. The authors acknowledge the computing center MesoLUM managed by ISMO

A Ar-Ar potential energy curves Phelps' model

$$0 < \rho < 3 : V(\rho) = \frac{Z_1 Z_2}{\rho^{1.5}} e^{-\rho/0.79}, \text{ where } Z_1 = Z_2 = 9.5 \quad (12a)$$

$$3 < \rho < 5 : V(\rho) = 61.6 \rho^{-4.5} \frac{e^{-(\frac{\rho}{5.5})^8}}{1 + (\frac{\rho}{5})^4} \quad (12b)$$

$$5 < \rho < \infty : V(\rho) = \epsilon \left[A e^{-\alpha x + \beta x} - F(x) \left(\frac{c_6}{x^6} + \frac{c_8}{x^8} + \frac{c_{10}}{x^{10}} \right) \right], \text{ where } \epsilon = 0.3359, x = \frac{\rho}{r_m} \text{ with } r_m = 7.107, \quad (12c)$$

$$A = 1.13211845 \times 10^5, \alpha = 9.00053441, \beta = -2.60270226, c_6 = 1.09971113 \\ c_8 = 0.54511632, c_{10} = 0.39278653 \text{ and}$$

$$F(x) = \begin{cases} e^{-(\frac{D}{x}-1)^2} & \text{for } x < D \\ 1 & \text{for } x > D \end{cases} \text{ with } D = 1.00400$$

Equations 12a to 12c show the analytical formulation of the inter-atomic potential between two atoms of argon [20], ρ denoting the relative distance between interacting atoms.

This form is in reasonable agreement with the computed ones for the Ar-Ar system [44]. On the one hand, the position of the well corresponds to about $7a_0$, where a_0 is the Bohr radius. On the other hand, for the Ti-Ar⁺ systems, the position of the wells covers the range from $5a_0$ to $6a_0$ [45]. This makes the $\gamma = 1.5$ factor not consistent with a crude rigid sphere model. Indeed there are many potentials energy curves involved in the Ti-Ar interaction due to the Ti open shell electronic structure as Ti=[Ar]3d²4s². But one can expect that the 4s electrons make certainly a resultant spherical shield that affects the 3d electrons, but is restricted only to a close interaction range. These 3d electrons are also expected to give also a quasi spherical shell, which makes relevant the approximation of spherical closed shell Ar-Ar potential energy curves of [20] to adjust the cross sections with a correcting factor. The deduced effective differential and total cross sections in figure 6 follow the expected 1/E behavior and allow a reasonable fit of the experimental data. The inversion procedures are very difficult when many potential energy curves are involved in the scattering problem [46]. The effective cross sections are a very interesting way to test and simulate *ab-initio* Ar-Ti computations that necessarily require further investigations.

B Test cases

Several studies have been performed to arrive at the best match possible between the experimental data and the results obtained from the model (see section 4). Depending on the cross section, the initial angular distribution, or on E_{max} in the modified Thompson, the results can vary significantly or only slightly differ. In this section additional cases are presented to better reflect the close match obtained between model and measurements. The table 2 shows the list of cases detailed here-below.

Figures 12 and 13 show the results obtained by the 3D MCC model if equations 6a and 6b are used, respectively, instead of equation 6c for the differential cross section. It corresponds the cases 1 and 2 in table 2, respectively. It is clear that from these two figures, none of the formula for the differential cross section (equations 6a and 6b) produce satisfactory results. Using equation 6b highly reduces the proportion of thermalized atoms and does not match the experimental curves. *A contrario*, using

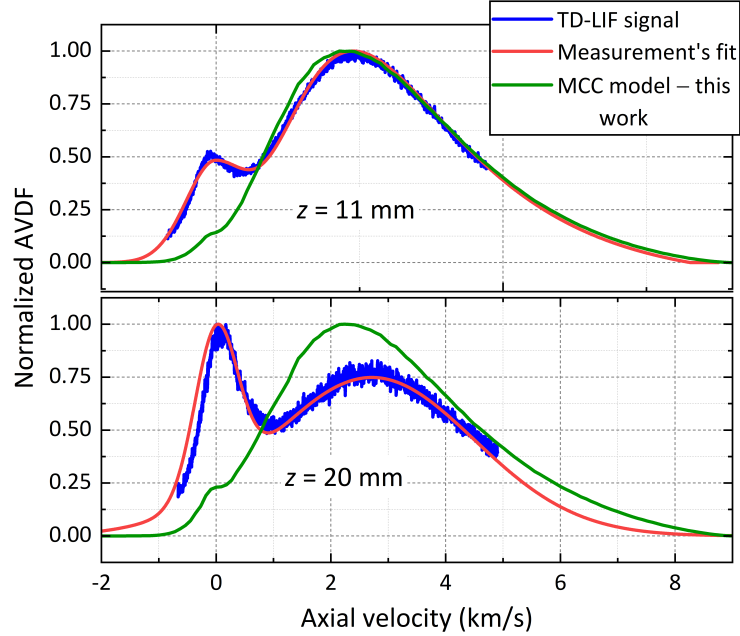


Figure 12: Velocity distribution function of the sputtered atoms (AVDF) of titanium for the case 1 listed in table 2 for two distances from the cathode. $\frac{d\sigma}{d\Omega}(\theta) = |f(\theta)|^2$.

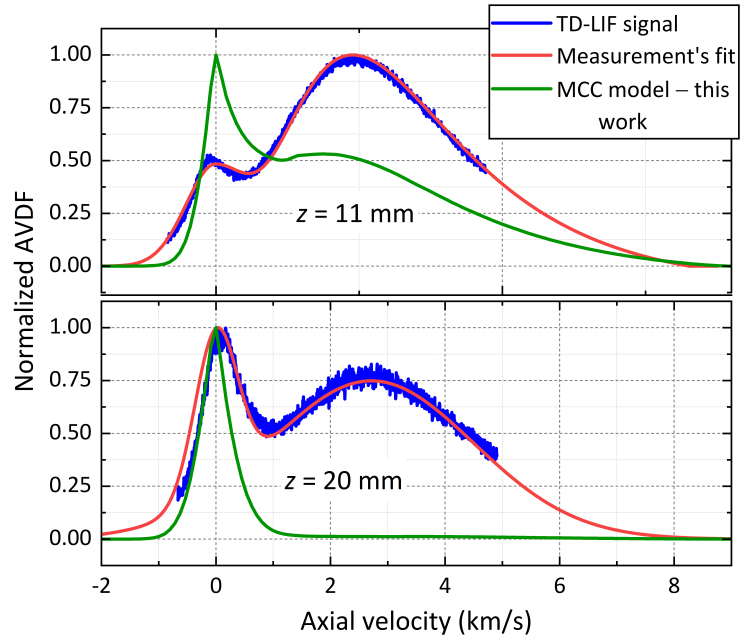


Figure 13: Velocity distribution function of the sputtered atoms (AVDF) of titanium for the case 2 listed in table 2 for two distances from the cathode. $\frac{d\sigma}{d\Omega}(\theta) = |f(\theta) + f(\pi - \theta)|^2$.

N	E_{\max} (eV)	Angle distribution	$\frac{d\sigma}{d\Omega}(\theta)$	T
1	20	$\cos\theta(1 + 2\cos^2\theta)$	$ f(\theta) ^2$	figure 3
2	20	$\cos\theta(1 + 2\cos^2\theta)$	$ f(\theta) + f(\pi - \theta) ^2$	figure 3
3	20	$\cos\theta(1 + 2\cos^2\theta)$	$1.5 f(\theta) ^2$	uniform (600 K)
4	20	$\cos\theta(1 + 10\cos^4\theta)$	$1.5 f(\theta) ^2$	figure 3
5	40	$\cos\theta(1 + 2\cos^2\theta)$	$1.5 f(\theta) ^2$	figure 3

Table 2: List of test cases.

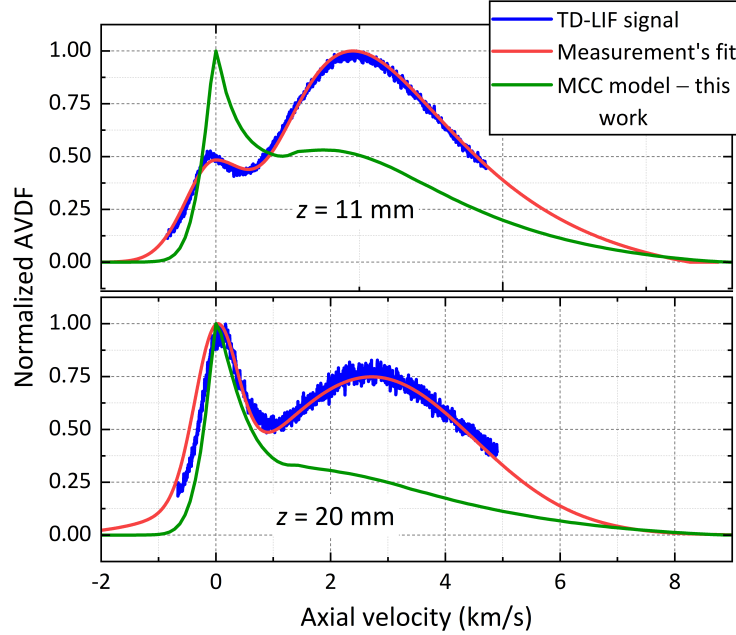


Figure 14: Velocity distribution function of the sputtered atoms (AVDF) of titanium for the case 3 listed in table 2 for two distances from the cathode. T uniform (600 K).

equation 6a increases the fraction of thermalized atoms so much that at $z = 11$ mm, almost all atoms are thermalized, in contradiction with TD-LIF measurements. The modified differential cross section formula (equation 6c) gives the best match between the model and the measurements. This is one of the contributions of the present paper.

Figure 14 shows the AVDF from the model if the temperature is assumed uniform in the whole simulation domain ($T = 600$ K). One can see that the proportion of thermalized atoms significantly increases. By keeping the temperature uniform close to the target, the density of neutral argon increases and so does the collision frequency. This result shows that it is critical to take into account the rarefaction effect, which is dependent of the magnetron cathode (target material, cooling system, etc.) and it translates in a significant variation (more than a factor of 2) of the neutral argon temperature close to the target compared to the one at thermal equilibrium.

Another parameter for the sputtered particles is the angular emission. Since the target is under constant ion bombardment, it is unclear at which angle the particles are emitted. Especially when the erosion track is well-installed and the target surface is not flat anymore. The angular distribution chosen in the main case of this work is $\cos\theta(1 + 2\cos^2\theta)$ (see figure 4(b)) but other distributions such as $\cos\theta(1 + 10\cos^4\theta)$ have also been tested. For the sake of example, this result is shown in figure 15. It only slightly differs from the result in figure 7.

The influence of the parameter E_{\max} in the equation 2 (modified Thompson energy distribution) has also been studied. Figure 16 shows the modeling results for $E_{\max} = 40$ eV. The results are here

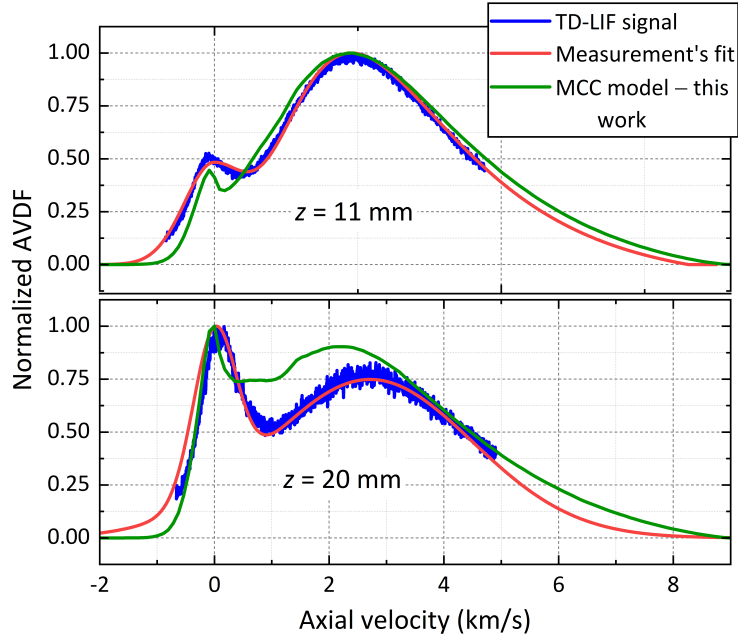


Figure 15: Velocity distribution function of the sputtered atoms (AVDF) of titanium for the case 4 listed in table 2 for two distances from the cathode. $\cos \theta(1 + 10 \cos^4 \theta)$.

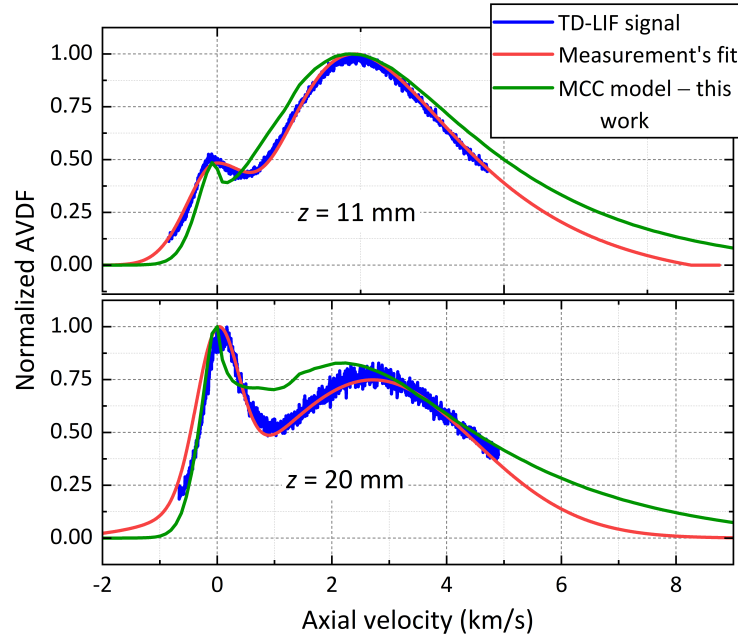


Figure 16: Velocity distribution function of the sputtered atoms (AVDF) of titanium for the case 5 listed in table 2 for two distances from the cathode. $E_{max} = 40$ eV.

also almost identical. As long as E_{max} is above 17 eV, this parameter has almost no effect on the AVDF.

C Fraction of metal vapor in DC magnetron discharge

The flux of Ar^+ , Γ_{Ar^+} , hitting the cathode can be expressed as $\Gamma_{\text{Ar}^+} = n_{\text{Ar}^+} v_B = n_{\text{Ar}^+} \sqrt{\frac{kT_e}{m_{\text{Ar}}}}$ where v_B is the Bohm velocity. The flux of Ti sputtered from the target is proportional to the flux of Ar^+ and can be expressed as $\Gamma_{\text{Ti}} = Y\Gamma_{\text{Ar}^+} = n_{\text{Ti}} v_{th} = n_{\text{Ti}} \sqrt{\frac{kT_{\text{Ti}}}{m_{\text{Ti}}}}$ where Y is the sputtering yield and v_{th} is the thermalized velocity of Ti.

By combining the equations, the ratio between the density of Ti and Ar can be obtained via $\frac{n_{\text{Ti}}}{n_{\text{Ar}^+}} = Y \sqrt{\frac{m_{\text{Ti}} T_e}{m_{\text{Ar}} T_{\text{Ti}}}}$. For a sputtering yield of 0.3 [47], and for $T_e \approx T_{\text{Ti}}$, this ratio is $\frac{n_{\text{Ti}}}{n_{\text{Ar}^+}} \approx 0.33$.

Consequently, the density of Ti is lower than the density of Ar^+ which is about 10^{16} to 10^{17} m^{-3} in DC regime [40]. Hence, the density of Ti is three orders of magnitude lower than the density of Ar (10^{20} m^{-3}). The Ti particles sputtered from the target are mainly affected by collision with neutral Argon and very sparingly by Ar^+ or by other Ti particles.

References

- [1] S. Rossnagel and J. Cuomo, “Film modification by low energy ion bombardment during deposition,” *Thin Solid Films*, vol. 171, no. 1, pp. 143–156, 1989.
- [2] D. Mattox, “Particle bombardment effects on thin-film deposition: A review,” *Journal of Vacuum Science & Technology A: Vacuum, Surfaces, and Films*, vol. 7, no. 3, pp. 1105–1114, 1989.
- [3] A. Anders, “A structure zone diagram including plasma-based deposition and ion etching,” *Thin Solid Films*, vol. 518, no. 15, pp. 4087–4090, 2010.
- [4] M. Desecures, L. De Poucques, and J. Bougdira, “Characterization of energetic and thermalized sputtered tungsten atoms using tuneable diode-laser induced fluorescence in direct current magnetron discharge,” *Plasma Sources Science and Technology*, vol. 24, no. 1, p. 015012, 2014.
- [5] D. Lundin, C. Vitelaru, L. d. Poucques, N. Brenning, and T. Minea, “Ti–Ar scattering cross sections by direct comparison of Monte Carlo simulations and laser-induced fluorescence spectroscopy in magnetron discharges,” *Journal of Physics D: Applied Physics*, vol. 46, p. 175201, May 2013.
- [6] C. Vitelaru, L. de Poucques, T. Hytkova, T. M. Minea, C. Boisse-Laporte, J. Bretagne, and G. Popa, “Pressure effect on the velocity and flux distributions of sputtered metal species in magnetron discharge measured by space-resolved tunable diode laser induced fluorescence,” *Plasma Processes and Polymers*, vol. 6, no. S1, pp. S326–S330, 2009.
- [7] C. Vitelaru, L. de Poucques, T. M. Minea, and G. Popa, “Space-resolved velocity and flux distributions of sputtered ti atoms in a planar circular magnetron discharge,” *Plasma Sources Science and Technology*, vol. 20, p. 045020, jul 2011.
- [8] M. Stepanova and S. Dew, “Anisotropic energies of sputtered atoms under oblique ion incidence,” *Nuclear Instruments and Methods in Physics Research Section B: Beam Interactions with Materials and Atoms*, vol. 215, no. 3, pp. 357–365, 2004.
- [9] T. Motohiro and Y. Taga, “Monte carlo simulation of thermalization process of sputtered particles,” *Surface Science Letters*, vol. 134, no. 1, pp. L494–L499, 1983.
- [10] T. Nakano and S. Baba, “Estimation of the pressure–distance product for thermalization in sputtering for some selected metal atoms by monte carlo simulation,” *Japanese Journal of Applied Physics*, vol. 53, no. 3, p. 038002, 2014.
- [11] G. M. Turner, I. S. Falconer, B. W. James, and D. R. McKenzie, “Monte carlo calculation of the thermalization of atoms sputtered from the cathode of a sputtering discharge,” *Journal of Applied Physics*, vol. 65, no. 9, pp. 3671–3679, 1989.
- [12] V. A. Volpyas, A. Y. Komlev, R. A. Platonov, and A. B. Kozyrev, “Thermalization of the flow of sputtered target atoms during ion-plasma deposition of films,” *Physics Letters A*, vol. 378, no. 43, pp. 3182–3184, 2014.
- [13] Y. Yamamura and M. Ishida, “Monte carlo simulation of the thermalization of sputtered atoms and reflected atoms in the magnetron sputtering discharge,” *Journal of Vacuum Science & Technology A*, vol. 13, no. 1, pp. 101–112, 1995.
- [14] K. Van Aeken, S. Mahieu, and D. Depla, “The metal flux from a rotating cylindrical magnetron: a monte carlo simulation,” *Journal of Physics D: Applied Physics*, vol. 41, no. 20, p. 205307, 2008.

- [15] D. Depla and W. Leroy, “Magnetron sputter deposition as visualized by monte carlo modeling,” *Thin Solid Films*, vol. 520, no. 20, pp. 6337–6354, 2012.
- [16] A. Caillard, C. Charles, R. Boswell, A. Meige, and P. Brault, “Deposition of platinum catalyst by plasma sputtering for fuel cells: 3d simulation and experiments,” *Plasma Sources Science and Technology*, vol. 17, no. 3, p. 035028, 2008.
- [17] R. Robinson, “Energetic binary collisions in rare gas plasmas,” *Journal of Vacuum Science & Technology*, vol. 16, no. 2, p. 185, 1979.
- [18] R. E. Somekh, “The thermalization of energetic atoms during the sputtering process,” *J. Vac. Sci. Technol. A*, vol. 2, p. 1285, 1984.
- [19] C. Vitelaru, D. Lundin, G. D. Stancu, N. Brenning, J. Bretagne, and T. Minea, “Argon metastables in HiPIMS: time-resolved tunable diode-laser diagnostics,” *Plasma Sources Science and Technology*, vol. 21, p. 025010, Apr. 2012.
- [20] A. V. Phelps, C. H. Greene, J. P. Burke, and A. V. Phelps, “Collision cross sections for argon atoms with argon atoms for energies from 0.01 eV to 10 keV,” *Journal of Physics B: Atomic, Molecular and Optical Physics*, vol. 33, pp. 2965–2981, Aug. 2000.
- [21] U. Deiters, “Monte carlo simulations of neon and argon using *ab initio* potentials,” *Molecular Physics*, vol. 98, pp. 1603–1616, 10 2000.
- [22] C. Costin, T. Minea, and G. Popa, “Electron transport in magnetrons by *a posteriori* monte carlo simulations,” *Plasma Sources Sci. Technol.*, vol. 23, p. 015012, 2014.
- [23] S. Kadlec, “Simulation of Neutral Particle Flow During High Power Magnetron Impulse,” *Plasma Processes and Polymers*, vol. 4, pp. S419–S423, Apr. 2007.
- [24] M. Fekete, J. Hnilica, C. Vitelaru, T. Minea, and P. Vašina, “Ti atom and ti ion number density evolution in standard and multi-pulse hipims,” *Journal of Physics D: Applied Physics*, vol. 50, no. 36, p. 365202, 2017.
- [25] J. Held, A. Hecimovic, A. von Keudell, and V. Schulz-von der Gathen, “Velocity distribution of titanium neutrals in the target region of high power impulse magnetron sputtering discharges,” *Plasma Sources Science and Technology*, vol. 27, no. 10, p. 105012, 2018.
- [26] P. Vasina, M. Fekete, J. Hnilica, P. Klein, L. Dosoudilová, P. Dvořák, and Z. Navrátil, “Determination of titanium atom and ion densities in sputter deposition plasmas by optical emission spectroscopy,” *Plasma Sources Science and Technology*, vol. 24, p. 065022, 11 2015.
- [27] M. Panjan and A. Anders, “Plasma potential of a moving ionization zone in dc magnetron sputtering,” *Journal of Applied Physics*, vol. 121, no. 6, p. 063302, 2017.
- [28] J. Bretagne, G. Delouya, and V. Puech, “High-energy electron distribution in an electron-beam-generated argon plasma,” *Journal of Physics D: Applied Physics*, vol. 14, no. 7, p. 1225, 1981.
- [29] J. Bretagne, J. Godart, and V. Puech, “Low-energy electron distribution in an electron-beam-generated argon plasma,” *Journal of Physics D: Applied Physics*, vol. 15, no. 11, p. 2205, 1982.
- [30] A. E. Farsy, D. Boivin, C. Noel, R. Hugon, S. Cuynet, J. Bougdira, and L. de Poucques, “Ionized particle transport in reactive HiPIMS discharge: correlation between the energy distribution functions of neutral and ionized atoms,” *Plasma Sources Science and Technology*, vol. 30, p. 065016, jun 2021.

- [31] A. E. Farsy, J. Ledig, M. Desecures, J. Bougdira, and L. de Poucques, “Characterization of transport of titanium neutral atoms sputtered in ar and ar/n2 HIPIMS discharges,” *Plasma Sources Science and Technology*, vol. 28, p. 035005, mar 2019.
- [32] M. Desecures, L. de Poucques, and J. Bougdira, “Characterization of energetic and thermalized sputtered tungsten atoms using tuneable diode-laser induced fluorescence in direct current magnetron discharge,” *Plasma Sources Science and Technology*, vol. 24, p. 015012, dec 2014.
- [33] C. Vitelaru, V. Pohoata, C. Aniculaesei, V. Tiron, and G. Popa, “The break-down of hyperfine structure coupling induced by the zeeman effect on aluminum $^2S_{1/2} \rightarrow ^2P_{1/2}$ transition, measured by tunable diode-laser induced fluorescence,” *Journal of Applied Physics*, vol. 109, no. 8, p. 084911, 2011.
- [34] M.-J. Lu, K. S. Hardman, J. D. Weinstein, and B. Zygelman, “Fine-structure-changing collisions in atomic titanium,” *Physical Review A*, vol. 77, no. 6, p. 060701, 2008.
- [35] G. D. Stancu, N. Brenning, C. Vitelaru, D. Lundin, and T. Minea, “Argon metastables in HiPIMS: validation of the ionization region model by direct comparison to time resolved tunable diode-laser diagnostics,” *Plasma Sources Science and Technology*, vol. 24, p. 045011, July 2015.
- [36] S. M. Rossnagel, “Gas density reduction effects in magnetrons,” *Journal of Vacuum Science & Technology A*, vol. 6, no. 1, pp. 19–24, 1988.
- [37] A. Revel, T. Minea, and C. Costin, “2D PIC-MCC simulations of magnetron plasma in HiPIMS regime with external circuit,” *Plasma Sources Science and Technology*, vol. 27, p. 105009, Oct. 2018.
- [38] V. Vahedi and M. Surendra, “A Monte Carlo collision model for the particle-in-cell method: applications to argon and oxygen discharges,” *Computer Physics Communications*, vol. 87, pp. 179–198, May 1995.
- [39] W. G. Vincenti and C. H. Kruger, *Introduction to physical gas dynamics*. 1965.
- [40] J. T. Gudmundsson, “Physics and technology of magnetron sputtering discharges,” *Plasma Sources Science and Technology*, vol. 29, p. 113001, nov 2020.
- [41] T. Mousel, W. Eckstein, and H. Gnaser, “Energy spectra of sputtered species under sub-keV ion bombardment: experiments and computer simulations,” *Nuclear Instruments and Methods in Physics Research Section B: Beam Interactions with Materials and Atoms*, vol. 152, no. 1, pp. 36–48, 1999.
- [42] T. Kozak and J. Lazar, “Gas rarefaction in high power impulse magnetron sputtering: comparison of a particle simulation and volume-averaged models,” *Plasma Sources Sci. Technol.*, vol. 27, no. 11, p. 115012, 2018.
- [43] C. Huo, D. Lundin, J. T. Gudmundsson, M. A. Raadu, J. W. Bradley, and N. Brenning, “Particle-balance models for pulsed sputtering magnetrons,” *Journal of Physics D: Applied Physics*, vol. 50, p. 354003, aug 2017.
- [44] P. Slavíček, R. Kalus, P. Paška, I. Odvárková, P. Hobza, and A. Malijevský, “State-of-the-art correlated ab initio potential energy curves for heavy rare gas dimers: Ar₂, Kr₂, and Xe₂,” *The Journal of Chemical Physics*, vol. 119, no. 4, pp. 2102–2119, 2003.

- [45] H. Partridge and C. W. Bauschlicher Jr, "Theoretical study of the low-lying states of TiHe^+ , TiNe^+ , TiAr^+ , VAr^+ , CrHe^+ , CrAr^+ , FeHe^+ , FeAr^+ , CoHe^+ , and CoAr^+ ," *The Journal of Physical Chemistry*, vol. 98, no. 9, pp. 2301–2306, 1994.
- [46] R. D. Levine, R. B. Bernstein, *et al.*, *Molecular reaction dynamics and chemical reactivity*. Oxford University Press, USA, Chap.3, 1987.
- [47] N. Matsunami, Y. Yamamura, Y. Itikawa, N. Itoh, Y. Kazumata, S. Miyagawa, K. Morita, R. Shimizu, and H. Tawara, *Energy dependence of the yields of ion-induced sputtering of monatomic solids*. 1983.